



# Phase Stability of Three Fe–Mn–Al–Ni Superelastic Alloys with Different Al:Ni Ratios

J. M. Vallejos<sup>1,2,3</sup> · M. F. Giordana<sup>1</sup> · C. E. Sobrero<sup>1,2,4</sup> · J. A. Malarria<sup>1,2</sup>

Received: 29 April 2021 / Revised: 26 May 2021 / Accepted: 30 May 2021  
© ASM International 2021

**Abstract** Fe–Mn–Al–Ni superelastic alloy is a potential candidate for diverse engineering applications due to its outstanding properties and low material costs. Recent studies suggest that slight changes in the chemical composition severely affect superelastic response, phase stability and grain growth kinetics. In this paper, we found that the Al stabilizes the parent  $\alpha$  phase at high temperature and promotes the formation of  $\beta$  precipitation at lower temperature. An alloy with a 3:1 ratio between Al and Ni produces homogeneously distributed  $\beta$  precipitates with high phase fraction in the alpha matrix after quenching from 1200 °C. The presence of these precipitates stabilizes the  $\alpha$  phase, lowers the martensitic transformation temperature and gives the alloy a fully-reversible stress-induced martensitic transformation behaviour without the need to apply an aging step. In alloys with lower Al content the  $\beta$  precipitation produced during quenching is severely restricted and pseudoelasticity is impaired.

**Keywords** Superelasticity · Pseudoelasticity · Thermoelastic · Fe–Mn–Al–Ni · Precipitation · Fe-based superelastic alloys

## Introduction

Over the past decade, iron-based superelastic alloys have grown in importance within the family of shape memory alloys (SMA) [1, 2]. Among these, Fe–Mn–Al–Ni presents large superelastic strains over a wide temperature range and good hot and cold workability. Due to these features, Fe–Mn–Al–Ni alloys have the potential to be used in aerospace, automotive and civil engineering applications [3]. In this system, a thermoelastic martensitic transformation occurs between a disordered body-centered cubic (A2 type) parent phase ( $\alpha$ ) and a face-centered cubic (A1 type) product phase ( $\gamma'$ ). The parent phase can be retained by water quenching from about 1200 °C. The presence of nanosized coherent B2-ordered NiAl-riched precipitates ( $\beta$ ) in the disordered  $\alpha$  matrix is necessary for a reversible stress-induced martensitic transformation. Conversely, the formation of a non-martensitic face-centered cubic phase ( $\gamma$ ) occurs under slow cooling rates from the  $\alpha$  phase field [4, 5].

A dislocation-based heterogeneous Bogers–Burgers model was proposed for the  $\alpha \rightarrow \gamma'$  martensitic transformation in the Fe–Mn–Al–Ni system [6] and a Pitsch-like orientation relationship was experimentally determined between  $\alpha$  and  $\gamma'$  phases [7]. The  $\beta$  precipitates play a key role in thermoelastic martensitic transformation. During  $\alpha \rightarrow \gamma'$  phase transition, the  $\beta$  precipitates are elastically distorted and the martensite is finely sheared by the introduction of nanotwins due to internal elastic strain, which is released during the reverse martensitic transformation

This article is part of a special topical focus in *Shape Memory and Superelasticity* on Fe-Based Shape Memory Alloys. This issue was organized by Dr. Toshihiro Omori and Dr. Ryosuke Kainuma, Tohoku University.

✉ J. A. Malarria  
malarria@ifir-conicet.gov.ar

<sup>1</sup> Instituto de Física Rosario, CONICET-Universidad Nacional de Rosario, Rosario, Argentina

<sup>2</sup> Facultad de Ciencias Exactas, Ingeniería y Agrimensura, Universidad Nacional de Rosario, Rosario, Argentina

<sup>3</sup> Facultad de Ingeniería, Universidad Nacional del Nordeste, Chaco, Argentina

<sup>4</sup> Institute of Materials Engineering, University of Kassel, Kassel, Germany

[8, 9]. In the martensite phase, twins are introduced with an average stacking order observed of 8 M and a  $5\sqrt{3}$  sequence. Recent studies suggest that  $\beta$  precipitates transform to a tetragonal  $L1_0$  phase during martensitic transformation [10]. This is also related to a tetragonal distortion of the  $\gamma'$  martensite phase [11].

The main drawback in this alloy is the strong and negative influence of the grain boundaries of the  $\alpha$  crystals on the superelastic effect [3, 12]. In samples with the average  $\alpha$  grain size smaller than the dimensions of the specimen, the superelastic recovery is severely restricted. Due to this, some novel processes for abnormal crystal growth were developed during the last years. Omori et al. applied a cyclic heat treatment (CHT) between two different temperatures: a high temperature where only the  $\alpha$  phase exists; and a lower temperature where both  $\alpha$  and  $\gamma$  phases coexist [4]. The  $\alpha$  subgrains formation, related to the precipitation of the  $\gamma$  phase during cooling, generates a dominant driving force that accelerates the grain growth of  $\alpha$  crystals, coarsening the  $\alpha$  grains in each cycle. Using a system for directional recrystallization [13], Vallejos and Malarria combined cyclic and directional heat treatments and achieved  $\alpha$  grains of  $\sim 8$  mm in 100 min in a Fe–Mn–Al–Ni alloy [14].

Several studies of the superelastic response under tension and compression were carried out in both bamboo-like microstructures [3, 12, 15–19] and  $\alpha$  single crystals [3, 18, 20–25]. While in tension the best performance was obtained in a single crystal oriented near  $\langle 011 \rangle_\alpha$  direction [3], in compression the central zone of the stereographic triangle appears to be the most suitable direction for maximize the superelastic effect [24]. In the opposite, the superelastic recovery strain appears to be low in crystals oriented in directions close to  $\langle 111 \rangle_\alpha$  [22, 24]. This is in correspondence with the theoretical calculations that predict the superelastic strain as a function of crystallographic orientation [6, 8, 23, 24].

Recent studies suggest that slight changes in the chemical composition of the Fe–Mn–Al–Ni system severely affect superelastic response, phase stability and grain growth kinetics. Vollmer et al. showed that the addition of small amounts of Ti drastically promotes the abnormal grain growth of  $\alpha$  crystals [26]. Xia et al. reported that the temperature dependence of the critical stress can be tuned by the addition of Cr [27]. This phenomenon was used for the authors to find a temperature-invariant stress-dependence Fe–Mn–Al–Ni–Cr alloy. Vallejos et al. showed that an alloy with higher Al content regarding the typical chemical composition (Fe–34Mn–15Al–7.5Ni in at.%) presents  $\beta$  precipitates of considerable size and homogenous distribution after quenching [14]. This allows to obtain a fully-reversible stress-induced

martensitic transformation without the aging conditioning step for  $\beta$  precipitation (typically at 200 °C for 3–6 h) carried out after quenching. A similar superelastic response was obtained by Xia et al. in an Al-rich Fe–Mn–Al–Ni alloy [28]. Based on thermodynamical calculations and experimental results, Walnsch et al. showed that the coherent  $\beta$  precipitates stabilize the parent  $\alpha$  state of the matrix and influence on the martensite start temperature ( $M_s$ ). Also, these results suggest that the chemical composition and volume fraction of the precipitates could influence on the thermoelastic martensitic transformation and superelastic response of the Fe–Mn–Al–Ni system. The present study focuses on the phase stability of three different Fe–Mn–Al–Ni alloys and the role of Al and Ni on the thermoelastic behaviour.

## Methodology

Three Fe–Mn–Al–Ni alloys with different chemical compositions were prepared by melting commercial raw materials under an argon atmosphere in an induction furnace and casting in ingots. These ingots were homogenized under an argon atmosphere at 1000 °C for 24 h. In order to evaluate the chemical composition of the alloys regarding Fe, Mn, Al and Ni elements, atomic absorption spectrometry studies were carried out. The direct combustion method was used to determine the C content. The chemical composition of the three alloys used in this study are summarized in Table 1.

Reduced portions of the ingots were cut with an electrical discharge machine. Then, some of these samples were hot-rolled at 1000 °C with a total thickness reduction of 50%. Also, a cold-rolled process with the same reduction that in the previous case was applied to some of the portions of the ingots.

In order to study the presence of the different phases at high temperature, the samples were subjected to a solution heat treatment (SHT) for 0.5 h at 1200 °C. The  $\alpha$  phase is expected to be the only stable phase at this temperature [3]. After the SHT, two different thermal routes were followed:

**Table 1** Chemical composition and nomenclature of the alloys studied in this work

Nomenclature	Element (at.%)				
	Fe	Mn	Al	Ni	C
17Al	Rest	33	17	6	0.15
15Al	Rest	34	15	7.5	0.1
11.5Al	Rest	38	11.5	7	0.15

- Room-temperature water quenching from 1200 °C.
- Slow cooling from 1200 to 1100 °C, holding this temperature for 0.5 h and then followed by a room-temperature water quenching.

The microstructures of the samples were studied by optical microscopy. The metallographic specimens were prepared using mechanical polishing techniques and etched with 7% nitric acid and 93% ethylic alcohol. The metallographic images were obtained with an Olympus PME3 optical microscope. The crystallographic orientations of the crystals were measured by electron backscatter diffraction (EBSD) with a FEI Quanta 200 FESEM Environmental and an Orientation Image Microscopy-EBSD system.

In order to study the thermoelastic cycle and phase transformation temperatures in the samples, several magnetization studies were carried out using a SQUID Quantum Design MPMS-5S magnetometer. The magnetization measurements were carried out using a magnetic field of 0.05 T. The size and distribution of  $\beta$  precipitates were investigated by transmission electron microscopy (TEM) using a JEOL JEM-2100Plus operated at 200 kV. TEM samples were prepared by double-jet electro-polishing with a solution of 950 ml acetic and 50 ml perchloric acid.

X-ray diffractograms and pole figure were measured using an Empyrean Panalytical X-ray diffractometer with a Cu tube and a monochromator at 40 kV and 40 mA. The Maud software was employed for Rietveld analysis of the diffraction patterns [29].

Specimens of  $3.5 \times 3.5 \times 60 \text{ mm}^3$  were subjected to the cyclic directional annealing (CDA) method in order to obtain abnormally grown  $\alpha$  grains [13, 14]. The procedure involves two iterations of cooling from an upper temperature of 1250 °C through a gradient of 68 °C/mm. Several drawing velocities were used in order to obtain different grain sizes in the specimens [14]. Prisms of  $2 \times 2 \times 3.5 \text{ mm}^3$  were obtained from these directionally annealed specimens using a diamond saw and mechanical polishing. In order to study the superelasticity of these samples, compression tests were performed in an Instron 3382 universal testing machine. The loading and unloading velocities were 0.1 mm/min and 0.5 mm/min, respectively. A 10 mm gauge length extensometer was used to measure the strain in the samples. For this, the arms of the sensors were in direct mechanical contact with the compression plates via knife edges.

## Results

The microstructures of 17Al, 15Al and 11.5Al alloys subjected to a SHT for 0.5 h at 1200 °C and then water quenching are shown in Fig. 1a–c, respectively. The 17Al

sample presents a fully  $\alpha$  microstructure of equiaxed grains of about 300  $\mu\text{m}$ . Similarly, the 15Al specimen shows  $\alpha$  grains surrounded by  $\gamma$  phase precipitated in the  $\alpha$  grain boundaries. A similar microstructure was first reported by Vollmer et al. [5] and it was attributed to a lower cooling rate than the one produced in cold water quenching, i.e., in hot water quenching. Also, some thin  $\gamma'$  martensite plates can be observed inside several  $\alpha$  grains in 15Al alloy. This may be a consequence of the stresses generated in the grains due to sudden cooling during quenching. As it is shown in Table 1, 11.5Al alloy presents higher Mn content than 15Al and 17Al alloys. Despite Mn stabilizes  $\gamma$  phase, it also has a strong effect on the hardness of  $\alpha$  ferrite. After quenching from 1200 °C, the 11.5Al alloy shows an  $\alpha + \gamma$  microstructure, with similar proportion between both phases. The  $\alpha$  grains range in size from 20 to 200  $\mu\text{m}$ . This implies that the complete solution of the  $\alpha$  phase did not occur at 1200 °C in this alloy. Figure 1d shows a metallography of 11.5Al sample quenched from 1200 °C with a higher magnification. Several  $\gamma'$  plates can be observed inside the  $\alpha$  crystals. Also,  $\gamma$  twins are shown in this figure. From these results, it is clear that 11.5Al chemical composition is not suitable as a superelastic alloy since a fully or almost fully  $\alpha$  microstructure cannot be achieved by water quenching from 1200 °C. In order to study the phase stability of the alloys at lower temperatures, after the SHT at 1200 °C, 17Al and 15Al samples were slowly cooled to 1100 °C, holding this temperature for 0.5 h and then quenched in room-temperature water. The metallographic images of 17Al and 15Al subjected to this heat treatment are shown in Fig. 1e and f, respectively. Both alloys present an  $\alpha + \gamma$  microstructure. However, the proportion of the  $\alpha$  phase is  $\sim 70\%$  in 17Al and  $\sim 50\%$  in 15Al. These results imply that the  $\alpha$  phase is more stable at high temperatures in 17Al alloy compared to 15Al alloy. This is expected since Al is the only  $\alpha$  stabilizer element in the Fe–Mn–Al–Ni system [30].

The X-ray diffraction patterns of 17Al, 15Al and 11.5Al alloys quenched from 1200 °C are shown in Fig. 2a–c, respectively. The 17Al sample presents high-intensity peaks corresponding to the  $\alpha$  phase. The smaller peaks indicate that some  $\gamma'$  exist in the sample. This may be a consequence of the stress generated in the grains due to the severe quenching or superficially induced during polishing. The diffractogram corresponding to 15Al specimen can be observed in Fig. 2b. In this case, the peaks corresponding to the face-centered cubic structure are remarkably higher than in 17Al alloy. Since the  $\gamma'$  martensite and the low temperature  $\gamma$  phase presents face-centered cubic structures with similar lattice parameters [3, 4], these cannot be distinguished from the X-ray diffraction data. Thus, the contribution of each of these phases in the peaks of Fig. 2b cannot be reliably determined. However, the



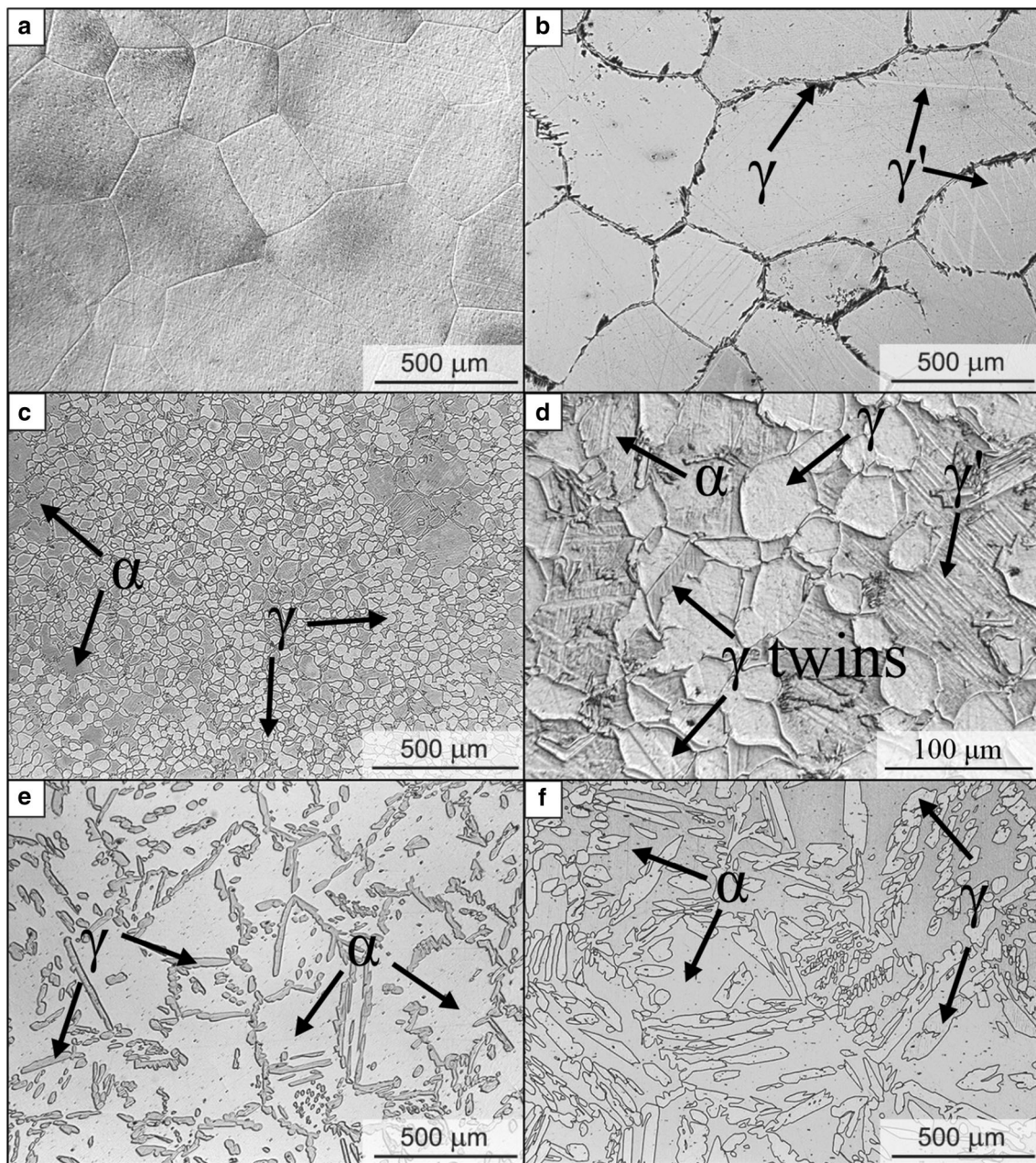


**Fig. 1** Metallographic images of the alloys subjected to a SHT at 1200 °C for 0.5 h and water quenching: **a** 17Al; **b** 15Al; **c** 11.5Al. **d** Image with higher magnification of the sample shown in **c**.

Metallographic images of the alloys subjected to a SHT at 1200 °C for 0.5 h, slowly cooled to 1100 °C and then water quenching: **e** 17Al; **f** 15Al

metallographic image shown in Fig. 1b indicates that the  $\gamma$  is only located in the grain boundaries of  $\alpha$  grains in 15Al alloy quenched from 1200 °C. For this, the major contribution of the diffraction peaks might arise from the  $\gamma'$  induced during quenching or polishing steps. This may indicate that in 15Al the  $\alpha$  phase is less stable than in 17Al since the  $\gamma'$  martensite is more easily induced in the former alloy. It is worth noting that in the diffractograms of 17Al and 15Al alloys, some peaks corresponding to  $\beta$  precipitates can be observed. Although many of the  $\beta$  peaks

coincide with the ones of the  $\alpha$  and  $\gamma/\gamma'$  phases, the diffractions of  $\{100\}_\beta$ ,  $\{200\}_\beta$  and  $\{210\}_\beta$  planes can be clearly observed in 17Al sample, and  $\{100\}_\beta$  and  $\{110\}_\beta$  diffractions peaks in 15Al sample. This confirms that the  $\beta$  precipitates are present in the Fe–Mn–Al–Ni system after quenching and without a low temperature aging step, as reported in our previous study [14]. Figure 2c shows the X-ray diffractogram corresponding to 11.5Al quenched from 1200 °C. In this specimen, the face-centered cubic peaks corresponding to  $\gamma$  and  $\gamma'$  phases are more intense

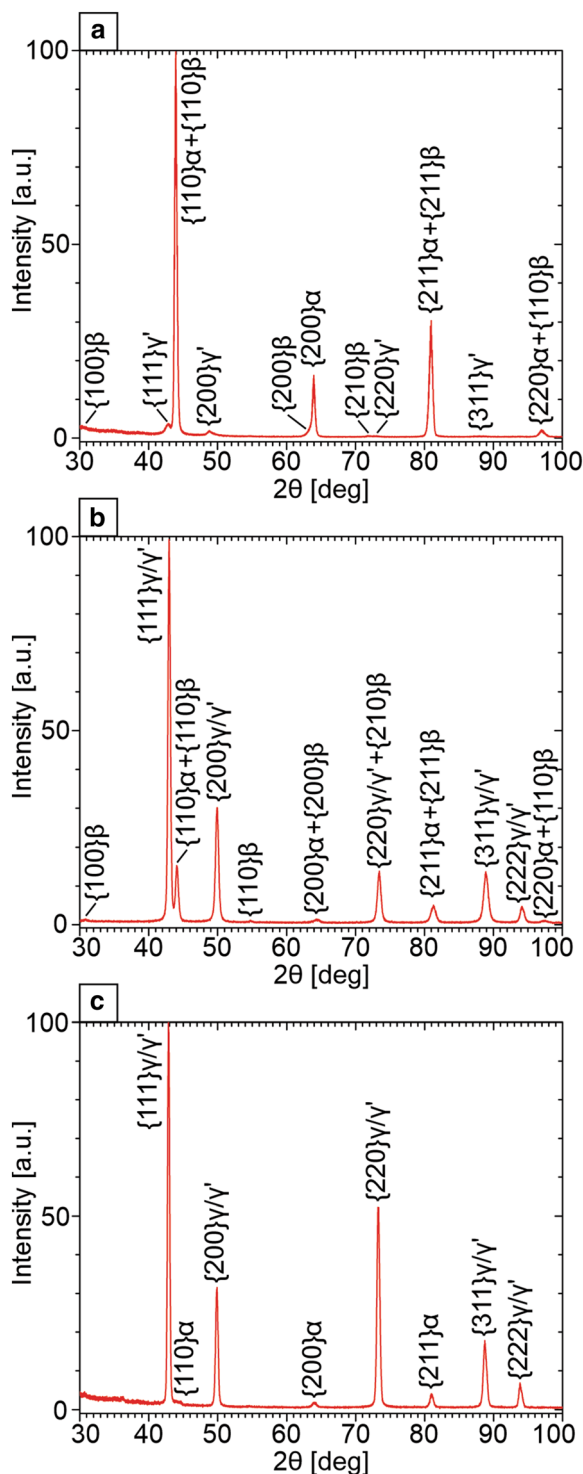


**Fig. 2** X-ray diffractograms of samples quenched from 1200 °C: **a** 17Al alloy; **b** 15Al alloy; **c** 11.5Al

than in the previous cases. This can be expected since the high volume of  $\gamma$  phase observed in Fig. 1c. Also, the many  $\gamma'$  plates inside the  $\alpha$  grains (Fig. 1d) indicate that the 11.5Al alloy is also prone to inducing martensite.

In order to calculate the lattice parameters of the  $\alpha$  phase ( $a_{\text{BCC}}$ ) in the three alloys studied, Rietveld refinements were carried out using the X-ray data shown in Fig. 2a–c. The  $a_{\text{BCC}}$  parameters obtained for the three alloys are summarized in Table 2. While  $a_{\text{BCC}}$  for 17Al and 15Al present very close values and are in correspondence with the one reported by Omori et al. [8], the  $\alpha$  lattice parameter for 11.5Al is significantly higher. This is expected since the 11.5Al has the lower Al content of the three alloys studied, which is the element with the smaller atomic radius in Fe–Mn–Al–Ni system [31].

The magnetization versus temperature of 15Al quenched from 1200 °C is shown in Fig. 3a. The  $\alpha \leftrightarrow \gamma'$  thermoelastic martensitic transformation was detected since a clear hysteresis loop can be observed. The decreasing in magnetization observed in cooling was attributed to the magnetic nature of the  $\alpha$  parent phase (ferromagnetic) and the  $\gamma'$  martensite phase (weak magnetic) [3]. For this, during the martensitic transformation the magnetization of the alloy is drastically reduced. The value of  $M_S$  is  $\sim -10$  °C, which is similar to the one reported by Omori et al. for a Fe–34Mn–15Al–7.5Ni (at. %) alloy [3]. Figure 3b shows the magnetization versus temperature of 15Al alloy quenched from 1200 °C and aging at 200 °C for 3 h. The hysteresis loop is no longer observed. This effect was also observed by Omori et al. [3] after an aging at 200 °C for 6 h, and it was attributed to the decreasing of  $M_S$  due to  $\beta$  precipitation. The magnetization versus temperature of 17Al quenched from 1200 °C is shown in Fig. 3c. A similar curve to the previous case is observed. Since no magnetization decreasing during cooling or hysteresis loop were detected in the study, it can be assumed that the  $M_S$  is below the lowest measured temperature ( $-253$  °C). It is worth noting that in this case no aging step was apply to the alloy after quenching. In order to study the magnetic nature of the martensite, a cold rolling with a total reduction of 90% was applied to a 17Al sample after quenching from 1200 °C. It is expected that a high amount of martensite was induced and retained after cold rolling. The magnetization curve as a function of temperature for this specimen is shown in Fig. 3d. A slight change in slope was detected in the magnetization curve at  $\sim -230$  °C. Since  $\gamma'$  martensite is paramagnetic, this temperature could be

**Table 2** Lattice parameter of the  $\alpha$  phase for the three alloys studied in samples quenched from 1200 °C

Alloy	$\alpha$ lattice parameter [nm]	Error [nm]
17Al	0.2904	0.0003
15Al	0.2903	0.0003
11.5Al	0.2914	0.0002



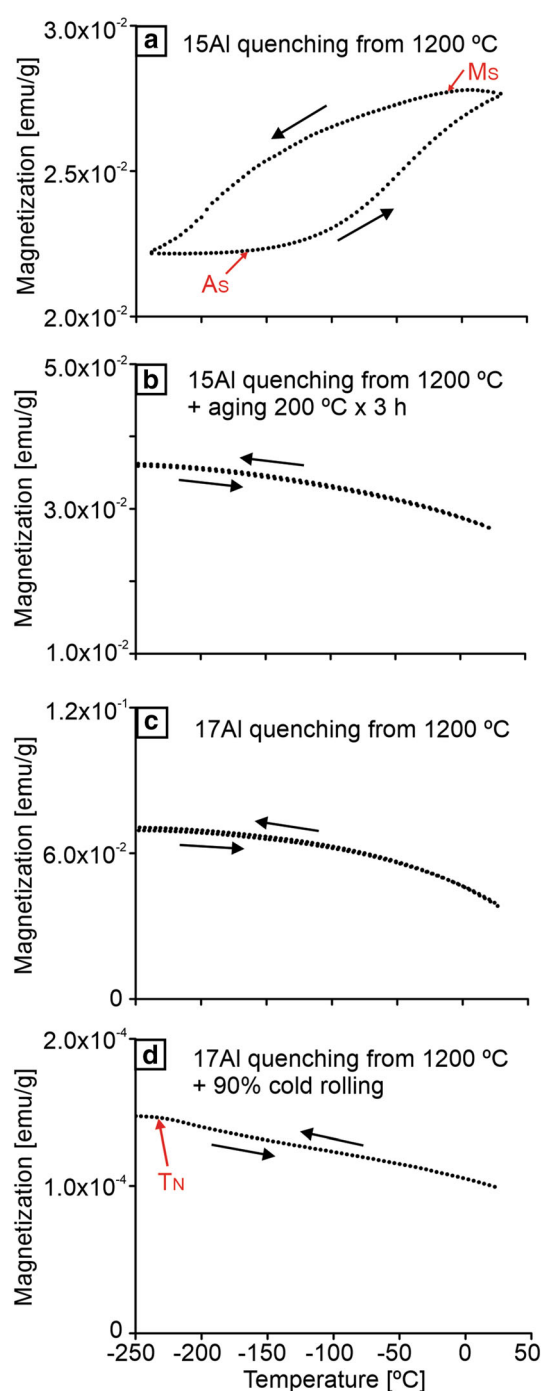


**Fig. 3** Magnetization vs. temperature curves for: **a** 15Al quenched from 1200 °C; **b** 15Al quenched from 1200 °C and further aging at 200 °C for 3 h; **c** 17Al quenched from 1200 °C; **d** 17Al quenched from 1200 °C and cold-rolled with a total reduction of 90%

identified as the Néel temperature ( $T_N$ ), at which this phase becomes antiferromagnetic on cooling.

In order to study the size and distribution of the  $\beta$  precipitates in the alloys for hot-rolled and quenching conditions, several TEM measurements were carried out. Figure 4a–c show the dark-field images of the precipitates

in hot-rolled 17Al, 15Al and 11.5Al specimens, respectively. The volume occupied by the  $\beta$  phase and its distribution homogeneity appears to be higher in 17Al than in 15Al and 11.5Al alloys. The 11.5Al alloy shows several small precipitates of about 1 nm and with the greater precipitates distributed in a few regions of the  $\alpha$  matrix, as can be seen in Fig. 4c. The dark-field images of 17Al and 15Al samples quenched from 1200 °C are shown in Fig. 4d and e, respectively. The 11.5Al alloy was not study in this condition since it is not possible to obtain a fully  $\alpha$  microstructure by quenching, as it is shown in Fig. 1c and d. Both 17Al and 15Al alloys show an increase in the size of the precipitates after quenching with respect to the hot-rolled condition. In order to obtain a statistically accurate size of the  $\beta$  phase, 500 precipitates were used for measurement in each analysed sample. The histograms showing the distribution of the precipitates size in 17Al, 15Al and 11.5Al alloys are shown in Fig. 4f–h, respectively. In 17Al alloy, a slight increment of the  $\beta$  precipitate sizes occur after quenching (Fig. 4f). Conversely, this increase in the size of the precipitates after quenching is remarkable greater in the 15Al alloy, as observed in Fig. 4g. In both alloys, the  $\beta$  size distribution in hot-rolled condition is represented by a lognormal function. On the other hand, in the quenched samples the distribution appears to be gaussian. The 11.5Al hot-rolled sample presents many precipitates with sizes in the range of 0.5–1.5 nm, as it can be observed in Fig. 4h. A secondary and lower peak is observed at  $\sim 3$  nm. The average size values and standard deviations of the  $\beta$  precipitates for 17Al and 15Al alloys in hot-rolled and quenched conditions are summarized in Table 3.

Finally, some incremental compression tests were carried out in 17Al samples with different average grain size and microstructure in order to investigate the superelastic response of the alloy. No further aging was applied after water quenching to any sample. The stress–strain curves are shown in Fig. 5a–c. The corresponding metallographic images showing the polycrystal microstructures of the samples tested are also plotted in Fig. 5a and b, below each stress–strain figure. In Fig. 5c, corresponding to a single crystal sample, the EBSD inverse pole figure (IPF) in load direction is also plotted. From Fig. 5a–c, it can be assumed that the shape recovery ratio (SRR) is increased with grain size in 17Al alloy. This effect was widely reported in Fe–34Mn–15Al–7.5Ni (at.%) alloy [3, 12, 16]. Also, the transformation stress ( $\sigma_{SE}$ ) reduces as the average size of the  $\alpha$  grains increases. There is a dramatic difference in the mechanical response of the cases shown in Fig. 5a and b. Despite the fact that the microstructure of both samples consists of a few coarse oligocrystals, the specimen shown in Fig. 5b presents courser crystals and, as a consequence, less grain boundaries that interfere with the activation and

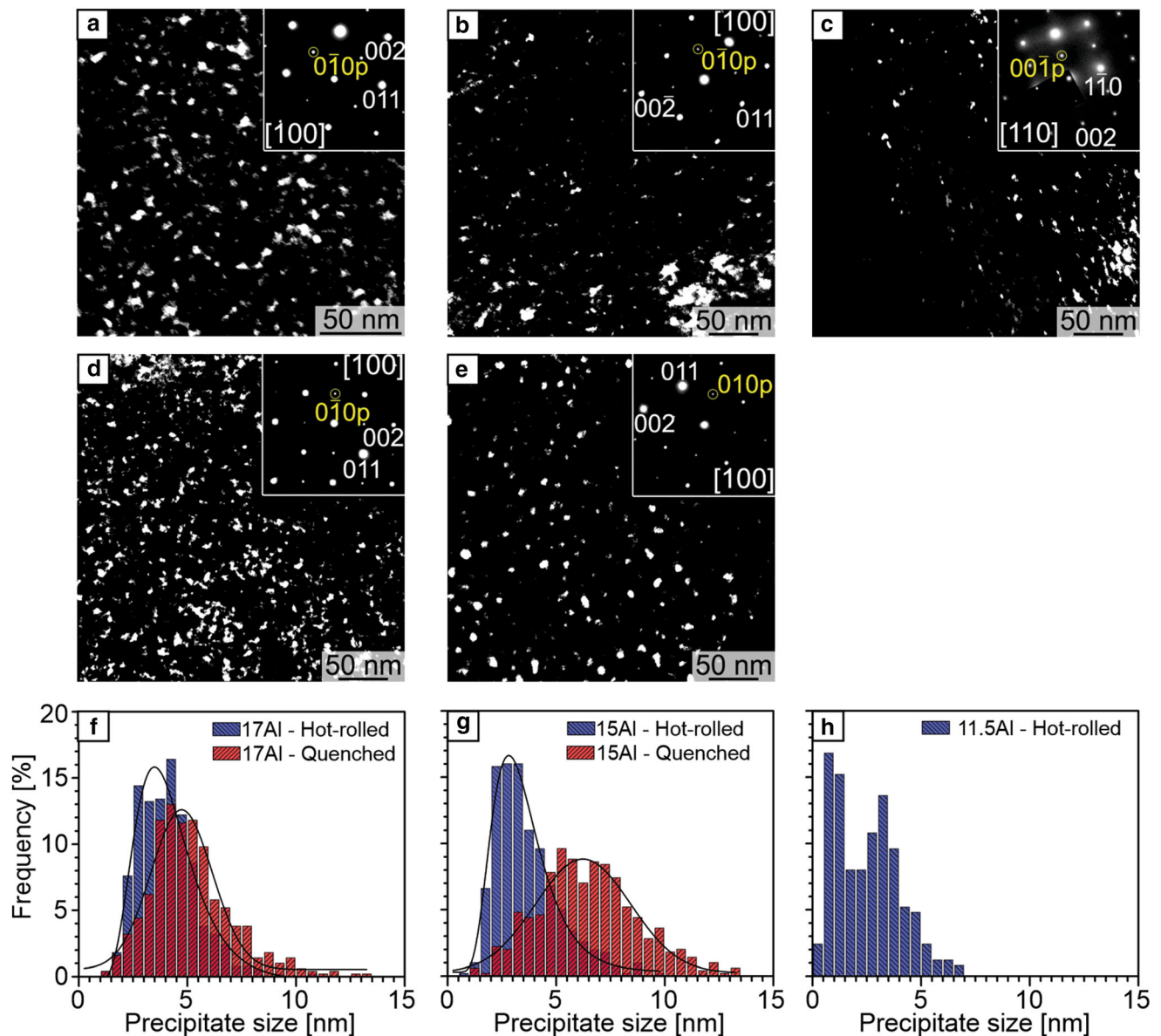


**Fig. 4** Dark field TEM images of  $\beta$  precipitates in: **a** 17Al hot-rolled; **b** 15Al hot-rolled; **c** 11.5Al hot-rolled; **d** 17Al quenched from 1200 °C; **e**. 15Al quenched from 1200 °C. **f–h** Histograms showing

the size distribution of precipitates in the hot-rolled and quenched conditions for 17Al, 15Al and 11.5Al, respectively

**Table 3** Average size and standard deviation of the  $\beta$  precipitates for 17Al and 15Al alloys in hot-rolled and quenched conditions

Sample—Thermomechanical condition	Average size [nm]	Standard deviation [nm]
17Al—hot-rolled	4.0	0.4
17Al—quenched	4.7	2.8
15Al—hot-rolled	3.3	0.4
15Al—quenched	6.2	4.4

shrinkage of the martensite. On the other hand, the single crystal shown in Fig. 5c presents an almost full-strain recovery performance. This excellent superelastic behaviour without a conditioning aging step in the alloy was

previously reported by the authors in several single crystals of 17Al alloy [24] and by Xia et al. in an Al-rich alloy [28].

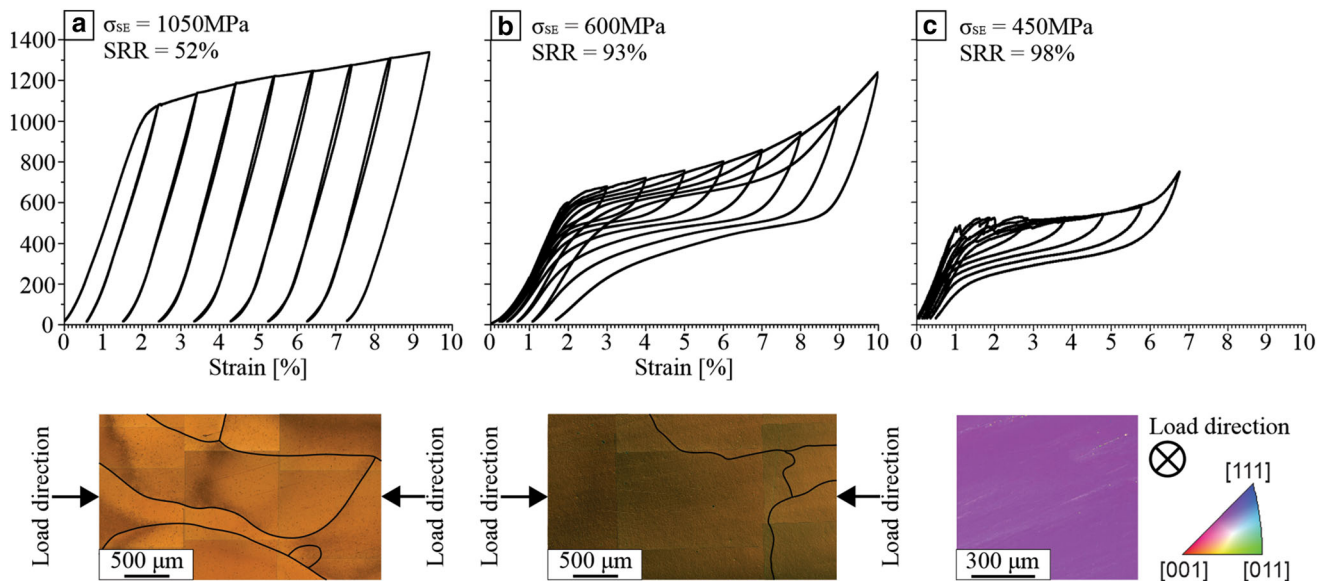


**Fig. 5** Stress–strain curves showing the superelastic response of 17Al alloy with three different microstructural conditions: **a** columnar-grained microstructure; **b** oligocrystalline microstructure; **c** single crystal

## Discussion

The phase stability in three different alloys of the Fe–Mn–Al–Ni system at high and low temperatures were studied in this paper. Since the Al is the only element in the system that stabilizes the  $\alpha$  “ferrite” parent phase, it plays a key role in obtaining a fully  $\alpha$  field at high temperatures [30]. From the metallographic images of the three alloys quenched from 1200 °C (Fig. 1a–d), it is clear that the Al content strongly influences the phase that are present in the alloy and their proportion in the microstructure. While in 17Al and 15Al samples a fully or almost fully  $\alpha$ -grained microstructure is obtained, in 11.5Al alloy an  $\alpha + \gamma$  biphasic microstructure is observed. Furthermore, at 1100 °C a higher proportion of  $\alpha$  phase is found in the 17Al alloy compared to the 15Al alloy, as shown in Fig. 1e and f, respectively. This confirms the stabilizing effect of Al on the  $\alpha$  phase at high temperatures.

For technological purposes it is interesting to find the lower limit of Al where a state of fully or almost fully  $\alpha$  grains is obtained by quenching from 1200 °C. Vollmer et al. achieved a bamboo-like  $\alpha$  microstructure in a Fe–Mn–Al–Ni alloy with 13.5% Al (at.%) by CHT followed by quenching in tempered water [15]. More recently, Walnsch et al. studied several chemical compositions and obtained a fully  $\alpha$  state by SHT at 1250 °C for 8 h followed by ice water quenching with 12.2% Al (at.%) in the alloy [10]. In this study, we failed in obtaining an  $\alpha$  grain microstructure in the 11.5Al alloy, as it is shown in Fig. 1c and d. The  $\alpha + \gamma$  microstructure was observed in this chemical composition even using 1250 °C as quenching temperature (for the sake of simplicity these results are not

shown in this paper). From the Fe–Mn–Al ternary system, it can be observed that the limit of the fully  $\alpha$  field at 1200 °C is  $\sim 12\%$  Al (at.%) [32]. From these results it can be concluded that the lower limit of Al to obtain a fully  $\alpha$  phase microstructure in Fe–Mn–Al–Ni quaternary system is around 12% Al (at.%).

From the diffraction pattern of Fig. 2a, it can be observed that the 17Al alloy quenched from 1200 °C presents a low volume fraction of  $\gamma'$  martensite. This phase is induced by the stress generated during the severe quenching and the polishing steps. In opposite, a more significative volume fraction of the  $\gamma'$  phase was identified in the 15Al alloy quenched from 1200 °C, as shown in the diffraction pattern of Fig. 2b. This is a strong indication that the 15Al alloy is more prone to thermally induce the  $\gamma'$  martensite than the 17Al alloy. The effect of the  $\alpha$  phase stabilization is more clearly observed in the magnetization vs. temperature curve for quenched 17Al alloy, as shown in Fig. 3c. No thermoelastic  $\alpha \rightarrow \gamma'$  martensitic transformation was identified in this measurement, which implies that the  $M_S$  for this alloy is below  $-250$  °C. Conversely, the 15Al alloy in quenched condition presents a clear thermoelastic hysteresis loop in the magnetization curve shown in Fig. 3a. In this case, the  $M_S$  is  $\sim -10$  °C, significantly higher than for the previous case. The remarkable difference in the undercooling observed in the two alloys implies that the 17Al alloy presents a more stable  $\alpha$  parent phase than the 15Al alloy. Thus, more energy must be applied in the former alloy to induce the  $\alpha \rightarrow \gamma'$  martensitic transformation.

The  $M_S$  calculated by Calphad for an Fe–34Mn–15Al–7.5Ni (at.%) alloy was  $\sim 900$  °C [33]. This value strongly



differs from the experimentally measured  $M_S$  [3, 9, 10, 34]. The difference was attributed to the thermodynamic contribution of the  $\beta$  precipitates to martensite formation [10]. This is a consequence of the positive Gibbs energy contribution due to the transformation of the B2 precipitates into  $L1_0$  structure. In this sense, the formation of  $\beta$  precipitates in the  $\alpha$  matrix seems to be responsible for the decreasing of  $M_S$ .

Despite the fact that  $\beta$  precipitates were observed in all the alloys studied, even in the hot-rolled condition, a significant growth in size and volume fraction occurs during quenching from 1200 °C, as can be seen in Fig. 4. The volume fraction of the precipitates before quenching appears to be higher as the Al content increases in the system, despite the fact that the sizes are similar, as observed in Fig. 4a–c. This effect of Al on the volume fraction seems to be maintained in the quenched condition. This is evidenced since in 17Al alloy the precipitates are smaller but more densely and homogeneously distributed than in 15Al alloy, as shown in Fig. 4d and e. The  $\beta$  precipitates not only contribute to the hardening of the  $\alpha$  matrix, but also play a fundamental role in the thermodynamics of the alloy by stabilizing the  $\alpha$  phase [10]. Contrary to previous studies that establish as a condition for obtaining a good superelastic effect in the alloy to have  $\beta$  precipitates of adequate size in the  $\alpha$  matrix, Walnsch et al. recently found that the  $\beta$  phase fraction significantly influences the Gibbs energy for  $\alpha \rightarrow \gamma'$  martensitic transformation and  $M_S$ . Thus, the higher the  $\beta$  phase fraction, the greater the energy contribution that stabilizes the  $\alpha$  phase and the lower  $M_S$ . This is consistent with our previous results, where we achieved an excellent superelastic effect and a fully-reversible stress-induced martensitic transformation with  $\beta$  precipitates of small size but with a homogeneous distribution and a high-volume fraction in the 17Al alloy [24]. This also explains the stability of the  $\alpha$  phase in the 17Al alloy compared to 15Al and 11.5Al alloys, since the fraction of precipitates is higher in the former one. It is also worth noting that the contribution of the  $\beta$  precipitates to the stability of the  $\alpha$  parent phase is drastically reduced as the Ni/Al ratio increases in the precipitates, as can be observed in Fig. 3b of Ref. [10]. Thus, it is expected that in an alloy with a Ni/Al ratio of 1:3, such as the 17Al, the  $\beta$  precipitates contain a higher proportion of Al than in the “classical” Fe–34Mn–15Al–7.5Ni (at.%) with a Ni:Al ratio of 1:2. The strong  $\alpha$  stabilization in 17Al alloy is clearly observed in the metallographic images shown in Fig. 1, the diffraction patterns of Fig. 2 and the magnetization vs. temperature curves of Fig. 3.

The miscibility gap that separates the  $\alpha$  (Fe-rich disordered A2) and  $\beta$  (NiAl-rich ordered B2) phases was firstly reported in ternary Fe–Ni–Al system [35] and is related to the  $\beta$  precipitation that occurs in superelastic Fe–Mn–Al–

Ni system [2]. In Fe–Al–Ni system, the miscibility gap is narrow at high temperatures and gradually broads as temperature decreases. The three-dimensional shape of the miscibility gap is a “Napoleon hat” type for this system, as can be seen in Fig. 9 of Ref. [35]. From this figure, it is clear that the Al content plays a key role on the temperature where the miscibility gap starts: the higher the Al content, the higher is the starting temperature of the miscibility region. If during quenching, the miscibility zone is reached at a higher temperature, more  $\beta$  phase fraction can be expected in the  $\alpha$  matrix due to the greater driving force available for precipitation [36]. This is in correspondence with the highest volume fraction of the  $\beta$  phase observed in Fe–Mn–Al–Ni alloys when the Al content is higher, as shown in Fig. 4a–e.

## Conclusions

In this paper we studied the phase stability of three different Fe–Mn–Al–Ni superelastic alloys. The chemical compositions of these alloys are Fe–33Mn–17Al–5Ni–0.15C (17Al), Fe–34Mn–15Al–7.5Ni–0.1C (15Al), and Fe–38Mn–11.5Al–7Ni–0.15C (11.5Al), expressed in at.%. The following conclusions can be drawn:

- At high temperatures, the Al content is related to the  $\alpha$  phase stability. A fully  $\alpha$ -grained microstructure can be generated by water quenching from 1200 °C in 17Al. While some  $\gamma$  formation occurs in  $\alpha$  grain boundaries during quenching in 15Al alloy, a biphasic  $\alpha + \gamma$  microstructure is obtained in 11.5Al. The lower limit of Al in the alloy to obtain a complete or almost complete  $\alpha$  grain structure after quenching from 1200 °C was set at around 12% Al.
- For the first time the coherent  $\beta$  precipitates were detected in the  $\alpha$  matrix in the Fe–Mn–Al–Ni system before quenching. In the hot-rolled condition, the 17Al alloy presented homogeneously distributed  $\beta$  precipitates with a higher fraction phase than in 15Al and 11.5Al alloys.
- The  $\beta$  precipitates volume fraction in the quenched condition presented a higher volume fraction for 17Al than for 15Al. This massive  $\beta$  precipitation after quenching in 17Al alloy is related to the stabilization of the  $\alpha$  phase, the lowering of the martensitic transformation temperature and the fully-reversible stress-induced martensitic transformation behaviour without the need to apply an aging step, observed in this alloy.
- The significative differences in phase stability and thermoelastic behaviour observed in the three samples studied in this paper, with relatively slight changes in

the chemical composition, highlight the importance of measuring the percentage of elements and controlling the manufacturing process, in homogeneities and segregations in ingots of Fe–Mn–Al–Ni alloys.

**Acknowledgements** The work presented in this paper was supported by the ANPCyT under Grant PICT-1460 and CONICET under Grants PDTs-251, PIP-0488 and PUE-096. The authors wish to express their gratitude to M. Melone for the magnetization measurements.

## References

- Chowdhury P, Canadinc D, Sehitoglu H (2017) On deformation behavior of Fe–Mn based structural alloys. *Mater Sci Eng R Rep*. <https://doi.org/10.1016/j.mser.2017.09.002>
- Omori T, Kainuma R (2017) Martensitic transformation and superelasticity in Fe–Mn–Al–based shape memory alloys. *Shape Mem Superelasticity*. <https://doi.org/10.1007/s40830-017-0129-9>
- Omori T, Ando K, Okano M, Xu X, Tanaka I, Onhuma R, Kainuma K (2011) Superelastic effect in polycrystalline ferrous alloys. *Science*. <https://doi.org/10.1126/science.1202232>
- Omori T, Iwazako R, Kainuma R (2016) Abnormal grain growth induced by cyclic heat treatment in Fe–Mn–Al–Ni superelastic alloy. *Mater Des*. <https://doi.org/10.1016/j.matdes.2016.04.011>
- Vollmer M, Segel C, Krooß P, Günther J, Tseng LW, Karaman I, Weidner A, Biermann H, Niendorf T (2015) On the effect of gamma phase formation on the pseudoelastic performance of polycrystalline Fe–Mn–Al–Ni shape memory alloys. *Scr Mater*. <https://doi.org/10.1016/j.scriptamat.2015.06.013>
- Ojha A, Sehitoglu H (2016) Transformation stress modeling in new Fe–Mn–Al–Ni shape memory alloy. *Int J of Plasticity*. <https://doi.org/10.1016/j.ijplas.2016.08.003>
- Vallejos JM, Sobrero CE, Ávalos M, Malarria JA (2018) Crystallographic orientation relationships in the  $\alpha \rightarrow \gamma'$  martensitic transformation in an Fe–Mn–Al–Ni system. *J of Appl Crystallography*. <https://doi.org/10.1107/S1600576718006738>
- Omori T, Nagasako M, Okano M, Endo K, Kainuma R (2012) Microstructure and martensitic transformation in the Fe–Mn–Al–Ni shape memory alloy with B2-type coherent fine particles. *Appl Phys Lett*. <https://doi.org/10.1063/1.4769375>
- La Roca P, Baruj B, Sobrero CE, Malarria JA, Sade M (2017) Nanoprecipitation effects on phase stability of Fe–Mn–Al–Ni alloys. *J of Alloys Compd*. <https://doi.org/10.1016/j.jallcom.2017.02.280>
- Walnsch A, Kriegel M, Motylenko M, Korpala G, Prah U, Leineweber A (2021) Thermodynamics of martensite formation in Fe–Mn–Al–Ni shape memory alloys. *Scr Mater*. <https://doi.org/10.1016/j.scriptamat.2020.10.003>
- Fischer P, Martin S, Walnsch A, Thümmel M, Kriegel M, Leineweber A (2021) Nanoscale twinning in Fe–Mn–Al–Ni martensite: a backscatter Kikuchi diffraction study. *J Appl Crystallogr*. <https://doi.org/10.1107/S1600576720013631>
- Omori T, Okano M, Kainuma R (2013) Effect of grain size on superelasticity in Fe–Mn–Al–Ni shape memory alloy wire. *APL Mater*. <https://doi.org/10.1063/1.4820429>
- Vallejos JM, Leonard ME, Sobrero CE, La Roca PM, Druker AV, Malarria JA (2017) Design, construction, and performance of a device for directional recrystallization of metallic alloys. *Rev Sci Instrum*. <https://doi.org/10.1063/1.4975179>
- Vallejos JM, Malarria JA (2020) Growing Fe–Mn–Al–Ni single crystals by combining directional annealing and thermal cycling. *J Mater Process Tech*. <https://doi.org/10.1016/j.jmatprotec.2019.116317>
- Vollmer M, Krooß P, Kriegel MJ, Klemm V, Somsen C, Ozcan H, Karaman I, Weidner A, Rafaja D, Biermann H, Niendorf T (2016) Cyclic degradation in bamboo-like Fe–Mn–Al–Ni shape memory alloys—the role of grain orientation. *Scr Mater*. <https://doi.org/10.1016/j.scriptamat.2015.12.007>
- Tseng LW, Ma J, Vollmer M, Krooß P, Niendorf T, Karaman I (2016) Effect of grain size on the superelastic response of a FeMnAlNi polycrystalline shape memory alloy. *Scr Mater*. <https://doi.org/10.1016/j.scriptamat.2016.07.036>
- Ozcan H, Ma J, Wang SJ, Karaman I, Chumlyakov Y, Brown J, Noebe RD (2017) Effects of cyclic heat treatment and aging on superelasticity in oligocrystalline Fe–Mn–Al–Ni shape memory alloy wires. *Scr Mater*. <https://doi.org/10.1016/j.scriptamat.2017.02.023>
- Vollmer M, Kriegel M, Walnsch A, Klemm V, Leineweber A, Niendorf T (2019) On the microstructural and functional stability of Fe–Mn–Al–Ni at ambient and elevated temperatures. *Scr Mater*. <https://doi.org/10.1016/j.scriptamat.2018.12.008>
- Poklonov VV, Kuksgauzen IV, Chumlyakov Y, Kuksgauzen DA, Kirillov VA (2020) Superelasticity and its cyclic stability in [001]-oriented single crystals and oligocrystals of FeMnAlNi alloy in compression. *Lett Mater*. <https://doi.org/10.22226/2410-3535-2020-1-78-82>
- Tseng LW, Ma J, Wang SJ, Karaman I, Kaya M, Luo ZP, Chumlyakov Y (2015) Superelastic response of a single crystalline FeMnAlNi shape memory alloy under tension and compression. *Acta Mater*. <https://doi.org/10.1016/j.actamat.2015.01.009>
- Tseng LW, Ma J, Wang SJ, Karaman I, Chumlyakov Y (2016) Effects of crystallographic orientation on the superelastic response of FeMnAlNi single crystals. *Scr Mater*. <https://doi.org/10.1016/j.scriptamat.2016.01.032>
- Poklonov VV, Chumlyakov Y, Kireeva IV, Kirillov VA (2018) Superelastic response in <1 2 2>-oriented single crystals of FeMnAlNi shape memory alloy in tension and compression. *Mater Lett*. <https://doi.org/10.1016/j.matlet.2018.09.015>
- Tseng LW, Ma J, Karaman I, Chumlyakov Y (2019) Orientation dependence of superelasticity in FeMnAlNi single crystals under compression. *Scr Mater*. <https://doi.org/10.1016/j.scriptamat.2019.02.034>
- Vallejos JM, Giordana MF, Sobrero CE, Malarria JA (2020) Excellent pseudoelasticity of Al-rich Fe–33Mn–17Al–6Ni–0.15C (at%) shape memory single crystals obtained without an aging conditioning stage. *Scr Mater*. <https://doi.org/10.1016/j.scriptamat.2019.12.038>
- Sidharth R, Wu Y, Brenne F, Abuzaid W, Sehitoglu H (2020) Relationship between functional fatigue and structural fatigue of iron-based shape memory alloy FeMnNiAl. *Shape Mem Superelasticity*. <https://doi.org/10.1007/s40830-020-00283-1>
- Vollmer M, Arold T, Kriegel MJ, Klemm V, Degener S, Freudenberger J, Niendorf T (2019) Promoting abnormal grain growth in Fe-based shape memory alloys through compositional adjustments. *Nat Commun*. <https://doi.org/10.1038/s41467-019-10308-8>
- Xia J, Noguchi Y, Xu X, Odaira T, Kimura Y, Nagasako M, Omori T, Kainuma R (2020) Iron-based superelastic alloys with near-constant critical stress temperature dependence. *Science*. <https://doi.org/10.1126/science.abc1590>
- Xia J, Omori T, Kainuma R (2020) Abnormal grain growth in Fe–Mn–Al–Ni shape memory alloy with higher Al content. *Scr Mater*. <https://doi.org/10.1016/j.scriptamat.2020.06.044>
- Lutterotti L, Matthies S, Wenk HR, Schultz AJ, Richardson J (1997) Combined texture and structure analysis of deformed

- limestone from time-of-flight neutron diffraction spectra. *J Appl Phys.* <https://doi.org/10.1063/1.364220>
30. Bain EC (1939) Alloying elements in steels, 1st edn. ASM, Cleveland
31. Vainshtein BK, Fridkin VM, Indenbom VL (1995) Structure of crystals, 3rd edn. Springer, Berlin
32. Umino R, Liu XJ, Sutou Y, Wang CP, Ohnuma I, Kainuma R, Ishida K (2005) Experimental determination and thermodynamic calculation of phase equilibria in the Fe–Mn–Al system. *J Phase Equilib Diffus.* <https://doi.org/10.1361/105497106X92817>
33. Walnsch A, Kriegel M, Fabrichnaya O, Leineweber A (2019) Thermodynamic assessment and experimental investigation of the systems Al–Fe–Mn and Al–Fe–Mn–Ni. *Calphad.* <https://doi.org/10.1016/j.calphad.2019.04.006>
34. Tseng LW, Ma J, Hornbuckle BC, Karaman I, Thompson GB, Luo ZP, Chumlyakov YI (2015) The effect of precipitates on the superelastic response of [100] oriented FeMnAlNi single crystals under compression. *Acta Mater.* <https://doi.org/10.1016/j.actamat.2015.06.061>
35. Hao SM, Takayama T, Ishida K, Nishizawa T (1984) Miscibility gap in Fe–Ni–Al and Fe–Ni–Al–Co systems. *Metall Trans A.* <https://doi.org/10.1007/BF02664895>
36. Chalmers B (1962) Physical metallurgy, 2nd edn. Wiley, New York

**Publisher's Note** Springer Nature remains neutral with regard to jurisdictional claims in published maps and institutional affiliations.